Manuscript prepared for Clim. Past
with version 2015/04/24 7.83 Copernicus papers of the LaTeX class copernicus.cls.
Date: 25 April 2016

The impact of the North American glacial topography on the evolution of the Eurasian ice sheet over the last glacial cycle

Johan Liakka[1], Marcus Löfverström[2], and Florence Colleoni[3]

[1]Biodiversity and Climate Research Centre, Senckenberg Gesellschaft für Naturforschung, Senckenberganlage 25, 60325 Frankfurt am Main, Germany.
[2]National Center for Atmospheric Research, 1850 Table Mesa Drive, 80305 Boulder, CO, USA.
[3]Centro Euro-Mediterraneo sui Cambiamenti Climatici, via Franceschini 31, 40128 Bologna, Italy.

Correspondence to: Johan Liakka (johan.liakka@senckenberg.de)

Abstract. Modeling studies have shown that the continental scale ice sheets in North America and Eurasia in the last glacial cycle had a large influence on the atmospheric circulation and thus yielded a climate distinctly different from the present. However, to what extent the two ice sheets influenced each others growth trajectories remains largely unexplored. In this study we investigate how an ice sheet in North America influences the downstream evolution of the Eurasian ice sheet, using a thermomechanical ice-sheet model forced by climate data from atmospheric snapshot experiments of three distinctly different phases of the last glacial cycle: the Marine Isotope Stages 5b, 4 and 2 (LGM). Owing to the large uncertainty associated with glacial changes of the Atlantic meridional overturning circulation, each atmospheric snapshot experiment was conducted using two distinctly different ocean heat transport representations. Our results suggest that changes in the North American paleo-topography may have largely controlled the zonal distribution of the Eurasian ice sheet. In the MIS4 and LGM experiments, the Eurasian ice sheet migrates westward towards the Atlantic sector – largely consistent with geological data and contemporary ice-sheet reconstructions – due to a low wavenumber stationary wave response, which yields a cooling in Europe and a warming in northeastern Siberia. The expansion of the North American ice sheet between MIS4 and LGM amplifies the Siberian warm anomaly, which limits the glaciation there and may therefore help explain the progressive westward migration of the Eurasian ice sheet in this time period. The ocean heat transport has only a small influence on the stationary wave response to the North American glacial topography; however, because temperature anomalies have a smaller influence on an ice sheet's ablation in a colder climate than in a warmer one, the impact of the North American glacial topography on the Eurasian ice-sheet evolution is reduced for colder surface conditions in the North Atlantic. While the Eurasian ice sheet in the MIS4 and LGM experiments appears to be in equilibrium with the simulated climate conditions, the MIS5b climate forcing is too warm to grow an ice sheet in Eurasia. First-order sensitivity experiments suggest that the MIS5b ice sheet was established during preceding colder stages.

1 Introduction

The Quaternary period is characterized by the alternation between cold and warm phases – glacial and interglacials – when massive ice sheets expand and retreat over the subpolar continents. The last glacial cycle began about 115 000 years ago (115 kyrs BP) following a minimum in the boreal summer insolation (Berger and Loutre, 1991). Over the subsequent ∼90 kyrs, paleo-records suggest that ice sheets progressively expanded in North America and Eurasia, with relatively rapid ice growth during colder phases followed by warmer periods when the global ice volume remained relatively constant (Peltier and Fairbanks, 2006; Stokes et al., 2012; Kleman et al., 2013). The colder phases are typically referred to as the Marine Isotope Stages (MIS) 5d (106-115 kyrs BP), 5b (85-93 kyrs BP), 4 (60-74 kyrs BP) and 2 (12-24 kyrs BP), where the latter includes the culmination of the last glacial cycle at the Last Glacial Maximum (LGM; 19-23 kyrs BP).

The progressive increase of the Northern Hemisphere ice volume was dominated by the Laurentide and Cordilleran ice sheets in North America (Kleman et al., 2013). Subsequent to the ice-sheet inception in the Canadian Arctic and Quebec, the Laurentide ice sheet expanded over the eastern parts of the continent and eventually coalesced with the Cordilleran ice sheet to form a coherent and continent-wide ice sheet at the LGM (Fig. 1; Clark et al., 1993; Kleman et al., 2010; Kleman et al., 2013). As opposed to the North American counterpart, the combined volume of the Eurasian ice sheets (Fennoscandian and Barents-Kara ice sheets) changed relatively little between the inception phase and LGM (Fig. 1; Svendsen et al., 2004; Kleman et al., 2013). Instead, the most notable feature of the ice-sheet evolution in Eurasia is a progressive westward migration in time; in the early and intermediate stages (MIS5b and MIS4) the eastern margin of the Eurasian ice sheet was located in central Siberia (Svendsen et al., 2004; Kleman et al., 2013), whereas essentially only northern Europe and the British Isles (Bradwell et al., 2008) were ice covered at the LGM (Fig. 1). Hence, in both North America and Eurasia, the ice sheets had strong zonal asymmetries toward the Atlantic sector over large parts of the glacial cycle. The driving mechanism of this asymmetry remains an open question as it has been difficult to capture this feature in conventional ice-sheet model experiments (Marshall et al., 2000; Zweck and Huybrechts, 2005; Charbit et al., 2007; Bonelli et al., 2009; Beghin et al., 2014).

The role of ice sheet-atmosphere interactions has mostly been studied for the build-up of the North American ice sheet (Roe and Lindzen, 2001; Liakka et al., 2011; Löfverström et al., 2014, 2015). These studies suggest that the east-heavy pre-LGM configuration arose from changes in the time-mean atmospheric circulation (stationary waves) forced by the ice sheet itself, possibly in combination with complex interactions with the North American Cordillera. The temporal evolution of the Eurasian ice sheet has received less attention. The orographic precipitation feedback, initially proposed by Sanberg and Oerlemans (1983), is generally considered an important feature to explain the westward migration of the ice sheet (Roe and Lindzen, 2001; Van Den Berg et al., 2008; Liakka and Nilsson, 2010; Kleman et al., 2013; Löfverström et al., 2014) as surface winds from the Atlantic

are forced vertically by the western and southern slopes of the ice sheet, hence leading to increased precipitation rates in those areas and ultimately to a (south)westward propagation of the ice sheet (Sanberg and Oerlemans, 1983). Although orographic precipitation is a robust feature in atmospheric general circulation models (Roe, 2005), questions regarding the timing of the westward migration of the ice sheet remain unanswered. For example, why did the Eurasian ice sheet propagate westward only in the latter stages of the glacial cycle and not immediately subsequent to the inception phase? The answer to this question is complicated by the fact that the orientation of the Atlantic storm track, which has a large impact on the European precipitation, appears to be controlled by the size of the North American ice sheet; for smaller ice sheets in North America (e.g. MIS5b and MIS4) the Atlantic storm track has a pronounced southwest-northeast tilt (similar to the modern climate Löfverström et al., 2014; Pausata and Löfverström, 2015), whereas for large ice sheets (LGM) the storm track has a more zonal orientation (Li and Battisti, 2008; Kageyama et al., 2013; Löfverström et al., 2014; Ullman et al., 2014; Merz et al., 2015; Pausata and Löfverström, 2015). The zonalisation of the Atlantic storm track typically yields drier (wetter) conditions in northern (southern) Europe (Löfverström et al., 2014).

The connection between the size of the Laurentide ice sheet and the orientation of the Atlantic storm track suggests that the North American glacial topography may have influenced the ice sheet evolution in Eurasia. Studies investigating remote climate impacts of the North American and Eurasian paleo-topography typically used static ice sheets as forcing in comprehensive circulation models (e.g. Li and Battisti, 2008; Löfverström et al., 2014; Ullman et al., 2014) or dynamic ice sheet models coupled to highly simplified atmospheric models (sometimes with parameterized climate anomalies Beghin et al., 2014). In this study, we investigate the effect of the geologically-constrained ice sheets in North America at MIS5b, MIS4 and LGM (see Fig. 1) on the evolution of the Eurasian ice sheet. The atmospheric response to the North American ice sheets is evaluated using a comprehensive atmospheric circulation model with nonlinear dynamics. The atmospheric fields are used as forcing in a thermomechanical ice-sheet model in order to evaluate their impact on the Eurasian ice sheet. More information about the models and the experiments is given in Section 2. In Section 3 we show the main results from the atmospheric and ice-sheet model experiments, followed by a comprehensive discussion in Section 4. Finally, the conclusions are summarized in Section 5.

2 Models and experiments

The successive experimental approach used here is summarized in Fig. 2. The details are provided below.

2.1 Atmospheric simulations

We use the climate snapshot (steady-state) simulations from Löfverström et al. (2014) representative for the pre-industrial (PI), MIS5b (88 kyrs BP), MIS4 (66 kyrs BP) and LGM (20 kyrs BP) climates. These experiments were conducted with the National Center for Atmospheric Research Community Atmospheric Model version 3 (NCAR CAM3; Collins et al., 2006) using T85 spectral resolution (approximately 1.4° horizontal resolution) and 26 hybrid levels in the vertical. Land surface processes are handled by the Community Land Model 3 (CLM3; Oleson et al., 2004). The ocean is represented by a mixed-layer (slab) model with a prescribed depth and ocean heat transport.

For each glacial time slice, we conduct two sets of simulations with different surface topography: (i) the reconstructed glacial topography from Kleman et al. (2013) (hereafter referred to as the "fullGlacial" simulations; see Fig. 1), and (ii) same as (i) except for using present-day topography in North America (hereafter referred to as the "EAonly" simulations). The impact of the North American ice sheet on the climate is evaluated as the difference between the fullGlacial and EAonly simulations. The orbital clock (Berger and Loutre, 1991) and greenhouse gas concentrations (Petit et al., 1999; Spahni et al., 2005) were adjusted to the nominal time of the ice-sheet reconstruction (Table 1). Other boundary conditions, e.g. aerosols, vegetation and landfraction were set to pre-industrial values; the latter two were properly adjusted for glaciated regions (Löfverström et al., 2014). As reference climate, we use an equilibrated present-day simulation from the same model (Hurrell et al., 2006). Results presented below are based on climatologies over 25 years after the simulated climates have reached statistical equilibrium.

2.1.1 Slab ocean model and ocean heat transport representations

We use a simplified slab (mixed-layer) ocean model in order to facilitate a high number of experiments, bracketing the uncertainty range in the planetary boundary conditions (see also Löfverström et al., 2014). The slab ocean model has a prognostic sea-surface temperature (SST) and a dynamic sea-ice edge calculated from the surface energy balance and the prescribed ocean heat transport (OHT) in the mixed layer (Collins et al., 2004; Bitz et al., 2012). Thus, the slab ocean model does not account for changes in ocean dynamics but retains the thermodynamic feedback between the ocean and the atmosphere.

The westerly mean flow implies that the North Atlantic sea-ice cover has a large influence on the temperature and moisture availability in Eurasia (e.g. Smith et al., 2003). The mean position of the North Atlantic sea-ice margin is in turn largely maintained by the Atlantic meridional overturning circulation (AMOC; Bitz et al., 2005). The strength of the LGM AMOC is the topic of ongoing research as it cannot be explicitly inferred from proxy-data evidence; modeling studies with coupled atmosphere-ocean models disagree on the LGM AMOC strength with some models suggesting that it was stronger than at present, whereas other models yield a weakening (Otto-Bliesner et al.,

2007; Weber et al., 2007). Following Löfverström et al. (2014), we therefore use two end-member representations of the OHT to bracket the uncertainty range of the AMOC strength. Both OHT representations are derived from equilibrated simulations with the (NCAR) Community Climate System Model version 3 (CCSM3), which is a fully-coupled model using CAM3 as atmospheric component. The first OHT representation, which represents a state of a relatively strong AMOC, stems from a pre-industrial simulation (hereafter referred to as "PI OHT"), and the second representation – representative for a weak AMOC state – from the LGM simulation in Brandefelt and Otto-Bliesner (2009) ("BO2009 OHT"). Note that we use the LGM2 rather than the LGM1 ocean state in Brandefelt and Otto-Bliesner (2009) because the LGM1 state (originally from Otto-Bliesner et al., 2006) is not in steady-state (Brandefelt and Otto-Bliesner, 2009). Unfortunately, the simulated LGM mixed-layer depth is not available on the CCSM3 data server; following Löfverström et al. (2014) we therefore use a modern annual mean mixed-layer depth in all simulations. Aside from areas covered by perennial sea ice, simulated changes of the LGM mixed-layer depth are however small compared to PI (of order 1-10 m; Brandefelt and Otto-Bliesner, 2009).

Changes in the simulated LGM AMOC have a large impact on the sea surface conditions in the North Atlantic; in CCSM3 (CAM3 with BO2009 OHT), the simulated AMOC is reduced with respect to the pre-industrial and the annual mean SSTs are substantially lower than contemporary proxy-based LGM SST reconstructions (Margo Project Members et al., 2009) resulting in a zonal sea-ice margin at $\sim$40°N (Fig. 3b; Brandefelt and Otto-Bliesner, 2009)[1]. In CCSM4 (Brady et al., 2013), on the other hand, the simulated LGM SSTs are significantly warmer than in CCSM3 and the sea-ice margin is located farther to the north in the eastern North Atlantic (Fig. 3c; Brady et al., 2013), thus in better agreement with LGM sea-ice reconstructions (Paul and Schäfer-Neth, 2003; Toracinta et al., 2004; De Vernal et al., 2005, 2006; Margo Project Members et al., 2009). The annual mean LGM SST response using the relatively strong PI OHT is in better agreement with the response in CCSM4 (and thus with the proxy) than in CCSM3 (Fig. 3a); for example, the sea-ice margin is located further north in the eastern North Atlantic (Fig. 3a). Therefore, we base the analysis on the simulations with PI OHT, whereas the simulations with BO2009 OHT are used in sensitivity experiments (Section 4.2).

2.2 Ice-sheet model

2.2.1 Model description

To simulate the evolution of the Eurasian ice sheet, we use the three-dimensional ice-sheet model SICOPOLIS (SImulation COde for POLythermal Ice Sheets, version 3.1), which treats ice as an incompressible, viscous and heat-conducting fluid (Greve, 1997). The model equations are subjected

[1]Note that the sea-ice cover in Fig. 3b is virtually identical to the one obtained in Brandefelt and Otto-Bliesner (2009) (see their Fig. 2), indicating that our slab ocean simulation is consistent with the fully-coupled simulation from which the OHT was derived.

to the shallow-ice approximation, which means that only the lowest order terms are retained (Hutter, 1983). The model obeys Glen's flow law to calculate strain rates (deformation) from the applied stresses (e.g. Van der Veen, 2013), and a Weertman-type sliding scheme to calculate the basal velocities (Weertman, 1964). Ice streams are not explicitly accounted for. We run the model in the "cold-ice mode", i.e. temperatures above the pressure melting point are artificially reset to the pressure melting temperature. Expansion of marine ice is allowed if the bathymetry is less than 500 m (default value), otherwise instant calving is assumed. The bedrock and overriding ice sheet are assumed to relax to isostatic equilibrium with a timescale of 3 kyrs, and the geothermal heat flux is 55 mW m^{-2} over the entire domain.

The surface mass balance is given by the difference between accumulation and ablation. In SICOPOLIS, accumulation is equal to precipitation and the ablation is parameterized using the positive degree day (PDD) approach (Braithwaite and Olesen, 1989; Reeh, 1991). The amount of PDDs in a year is given by the integrated sum of positive temperatures over that year, and is evaluated using the semi-analytical solution in Calov and Greve (2005). It is assumed that the daily temperatures in a month are normally distributed about the monthly-mean temperature. The standard deviation (day-to-day variability) of the temperature is 5°C everywhere (default). We use the default values of the degree-day constants, which relate the PDDs to actual melt rates (3 mm day^{-1} K^{-1} for snow and 12 mm day^{-1} K^{-1} for ice). The melting procedure follows Reeh (1991). First the PDDs are used to melt the annual snow fall. It is assumed that 60% of that melt water percolates into the ice and contributes to the formation of superimposed ice. Second, the superimposed ice is melted, after which the remaining PDDs, if any, are used to melt the glacier ice.

Following Charbit et al. (2002) and Charbit et al. (2007), the surface temperature (T) and precipitation (P) over the evolving ice sheet are modified according to a fixed atmospheric lapse rate γ:

$$T(t) = T_0 + \gamma(z(t) - z_0), \quad (1)$$

$$P(t) = P_0 \exp(\gamma_s \gamma(z(t) - z_0)), \quad (2)$$

where $z(t)$ is the height of the evolving ice-sheet surface (t =time), and T_0 and P_0 are the reference temperature and precipitation on the initial ice-free topography z_0, respectively (see Eqs. 3 and 4 in Section 2.2.2). Hence, it is assumed that the temperature decreases linearly with height z at the lapse rate γ (set to value of the standard atmosphere: $\gamma = -6.5 \times 10^{-3}$ K m^{-1}), and that precipitation decreases exponentially with the temperature change (due to elevation) times the parameter γ_s, which relates the temperature anomaly to precipitation change (set to $\gamma_s = 0.05$ K^{-1} following Charbit et al., 2002, 2007). Because the surface temperature on the ice sheet is evolving in time, the relative amount of solid and liquid precipitation is parameterized; following Marsiat (1994), the fraction snowfall to the total precipitation is one if the monthly-mean air temperature is below -10°C, and zero if it is greater than 7°C. For intermediate temperatures the fraction snowfall is linearly interpolated.

2.2.2 Experimental design and initial climate forcing

The SICOPOLIS simulations are carried out to steady-state (at least 150 kyrs) from an ice-free initial state using the CAM3 simulations as climate forcing. The horizontal resolution is set to 80 km, and the model domain covers most of the Northern Hemisphere. The relatively coarse horizontal resolution is motivated by the fact that we are interested in large scale first-order changes of the Eurasian ice sheet (as reference, Kleman et al., 2013, used a horizontal resolution of 95 km in their ice-sheet reconstructions). The vertical resolution amounts to 81 levels in the ice and 11 levels in the bedrock.

We use the procedure described in Charbit et al. (2007) to deduce the initial fields of surface temperature (T_0) and precipitation (P_0) from the atmospheric model:

$$T_0 = T_{PD,obs} + T_{paleo,CAM} - T_{PD,CAM} - \gamma(z_{paleo} - z_{PD}), \quad (3)$$

$$P_0 = P_{PD,obs} \times (P_{paleo,CAM}/P_{PD,CAM}) \times \exp[-\gamma_s \gamma(z_{paleo} - z_{PD})]. \quad (4)$$

To account for systematic biases in the atmospheric climatology we first calculate anomalies of the glacial temperature ($T_{paleo,CAM}$) with respect to the temperature of the present-day simulation ($T_{PD,CAM}$). In doing so, we correct for the different orographies in the glacial and present-day simulations ($z_{paleo,CAM}$ and $z_{PD,CAM}$, respectively) using the standard lapse rate. Subsequently, the anomalies are bi-linearly interpolated to the SICOPOLIS grid and added to the observational dataset ($T_{PD,obs}$), which is based on ERA-Interim reanalysis data (Dee et al., 2011). To calculate P_0 we use the same technique as for T_0, but we use ratios instead of anomalies in order to omit negative precipitation (Charbit et al., 2007).

3 Results

3.1 Atmospheric response

3.1.1 Summer temperature

The annual ablation is dominated by the summer conditions; we therefore focus on the surface temperature in boreal summer (June–August: JJA). Figure 2 shows the JJA surface temperature in the reanalysis data (a), present-day simulation (b) and the EAonly paleo simulations (c,e,g). To highlight areas susceptible for inception, the temperatures in Fig. 4 are projected to the present-day orography using the standard lapse rate. A summary of the average summer temperatures in the Northern Hemisphere and Eurasia is presented in Table 2.

The average Northern Hemisphere summer temperature decreases across the EAonly simulations; it drops by 3°C between present-day and MIS5b, and by an additional 2°C at LGM (Table 2). The cooling across the glacial simulations has even larger regional variations: in Eurasia, the LGM summer temperature is about 5°C lower than at MIS5b (Table 2). Regions with sub-freezing summer

temperatures are particularly interesting for glacial inception; the average position of the zero-degree summer (surface) isotherm in indicated by the green contour in Fig. 4a,b,c,e,g. Similar to present-day (Fig. 4a,b), the zero-degree isotherm at MIS5b is mainly located in the Arctic Ocean poleward of the Eurasian continent (Fig. 4c). Owing to the cooler conditions at MIS4 and LGM, the (zonal) average location of the zero-degree isotherm is shifted equatorward by 6 to 7° (Table 2); the largest regional changes are found in Scandinavia and eastern Siberia, where it reaches as far south as 60°N at MIS4 and LGM (Fig. 4e,g).

Figure 4d,f,h shows the summer (surface) temperature anomalies induced by the North American ice sheet. These anomalies are calculated as the difference between the fullGlacial and EAonly simulations; a lapse rate correction has been applied to account for elevation differences. Due to an increased surface albedo and cold air advection by orographically-forced stationary waves (Cook and Held, 1988; Roe and Lindzen, 2001; Abe-Ouchi et al., 2007; Liakka and Nilsson, 2010; Liakka, 2012; Löfverström et al., 2015), the largest cooling occurs in the vicinity of the North American ice sheet. In Eurasia, the temperature response to the North American ice sheet exhibits large regional variations. For all time slices, the North American ice sheet induces colder conditions in Europe. The response in Siberia is more complicated; at MIS5b the Siberian temperature response is almost negligible (Fig. 4d), whereas there is a warming in eastern Siberia at MIS4 and LGM. The largest difference between the MIS4 and LGM responses is found in central Siberia, which becomes colder at MIS4 (Fig. 4f) and warmer at LGM (Fig. 4h).

3.1.2 Annual precipitation

The large-scale features of the annual precipitation in the EAonly simulations are reminiscent of the modern climate, although the global precipitation rates are somewhat reduced in the glacial simulations (Fig. 5a,b,c,e,g). The largest precipitation rates in Eurasia are found in northwestern Europe where the cyclones from the Atlantic stormtrack make landfall.

As for the temperature, the largest precipitation response to the North American ice sheet is found over the ice sheet itself, with generally increased precipitation on the windward (westerly) slopes of the ice sheet and reduced precipitation over the leeward (easterly) slopes (Fig. 5d,f,h). In Eurasia, the North American ice sheet has a relatively small impact on the precipitation at MIS5b and MIS4 (Fig. 5d,f), but yields a significantly reduced precipitation in northwestern Europe at LGM (Fig. 5h). As discussed in Löfverström et al. (2014), the reduced precipitation rates at LGM is associated with a zonalisation of the midlatitude Atlantic jet stream resulting from flow-topography interactions with the continent-wide North American ice sheet (Li and Battisti, 2008; Ullman et al., 2014; Merz et al., 2015; Pausata and Löfverström, 2015). Löfverström et al. (2014) found that this effect is not present for the smaller pre-LGM ice sheets (MIS5b and MIS4), as their location and spatial extent allow the mean-flow to largely circumvent the topography, thus rendering the tilt of the Atlantic jet – and stormtrack – largely similar to the present-day.

3.1.3 Summer stationary waves

In order to understand the temperature response in Fig. 4, we examine the stationary Rossby waves in the different climate states. Stationary waves, defined as zonal asymmetries in the climatological fields, are the result of large scale orography and diabatic heating (e.g. Hoskins and Karoly, 1981; Held et al., 2002; Held, 1983; Kaspi and Schneider, 2011). Ice sheets constitute both orographic and diabatic forcing of stationary waves. Therefore, ice sheets expanding into the westerly mean flow can potentially influence the global stationary wave field (e.g. Cook and Held, 1988; Roe and Lindzen, 2001; Löfverström et al., 2014).

The lower troposphere (700 hPa) geopotential height anomalies from the EAonly simulations are shown in Fig. 6c,e,g. The stationary wave response is qualitatively similar in all glacial time slices; similar to the modern climate (Fig. 6a,b), the summer stationary wave field is characterized by anticyclonic circulation (ridges) over the subtropical Pacific and Atlantic ocean basins, and cyclonic circulation (troughs) over Asia and northeastern Canada (Fig. 6c,e,g). In addition, the ridge over the Atlantic Ocean extends over Europe and covers most of the ice sheet area, suggesting that the local ridge is excited by the Eurasian ice sheet. As noted by Löfverström et al. (2014), this indicates that the ice sheet's diabatic cooling is dominating the stationary wave response.

The 700 hPa geopotential height responses to the North American ice sheets are shown as shading in Fig. 6d,f,h. As expected from theory, the stationary wave amplitudes increases with the size (spatial extent and height) of the North American ice sheet (Cook and Held, 1992; Ringler and Cook, 1997; Liakka and Nilsson, 2010; Liakka et al., 2011; Löfverström et al., 2014). Besides the amplitude, the stationary wave response to the North American ice sheet is qualitatively similar in all time slices. The local response is a ridge over the northwestern parts of the North American ice sheet and a trough in the southeast. This particular response is a robust feature across models using nonlinear stationary wave dynamics (Ringler and Cook, 1997, 1999; Liakka et al., 2011). The remote downstream response consists of two wavetrains: (i) a subtropical wavetrain with a northwest-southeast orientation, and (ii) a low wavenumber polar wavetrain with a more zonal orientation. The polar wavetrain is characterized by a trough over Europe/western Asia and a ridge over Siberia.

The contours in Fig. 6d,f,h depict the geopotential height anomalies at 300 hPa. The anomalies at this level have essentially the same spatial location as at 700 hPa, indicating that the climatological response to the North American ice sheet is largely equivalent barotropic.

In the summer season, high-latitude geopotential height anomalies are typically well correlated with surface temperature anomalies. Ridges are associated with reduced cloudiness and increased downwelling shortwave radiation, which leads to a surface warming, whereas troughs typically yield increased cloudiness and thus lower surface temperatures. This is also seen here (cf. Fig. 4d,f,h and 6d,f,h): the ridge over eastern Siberia and Alaska is associated with a surface warming, and the trough in Europe with a cooling. Note that the magnitude of these temperature anomalies, in

particular the Siberian warm anomaly, is not only controlled by the geopotential height anomalies, but also by albedo feedbacks due to changes in the snow cover (see Fig. 1 in the Supplement).

3.2 Ice-sheet evolution

In this section we examine how the altered climate conditions – induced by the North American ice sheet – influence the spatial equilibrium extent of the Eurasian ice sheet. To evaluate our results, we compare the simulated extents of the Eurasian ice sheet with the geologically-constrained reconstructions from Kleman et al. (2013). Note that we only compare the geographical distribution of ice (i.e. ice area), but not the ice thickness or ice volume. The reason is that the ice thickness in the Kleman et al. (2013) reconstructions is a model dependent feature, whereas the spatial extents are constrained by geological evidence.

Figure 7 shows the simulated equilibrium ice thickness when using the atmospheric simulations summarized in Figs. 4 and 5 as climate forcing. Apart from some ice caps in the Scandinavian mountains, Eurasia remains ice free at MIS5b (Fig. 7a,b). This is consistent with a negative surface mass balance over essentially the entire domain (Fig. 2 in the Supplement). A comprehensive discussion on the potential shortcomings in the MIS5b simulations follows in section 4.3.

At MIS4 and LGM, atmospheric circulation changes induced by the North American ice sheet serves to increase the total ice area in Eurasia by about 80% and 30%, respectively (Fig. 7). This increase is mediated by an expansion of ice in western Eurasia and a reduced ice extent in eastern Siberia; apart from slightly too much ice in the Kara-sea region in the LGM simulation, the outlines of the simulated MIS4 and LGM ice sheets in Eurasia are in good agreement with the reconstructions from Svendsen et al. (2004) and Kleman et al. (2013); see Fig. 7d,f. In the absence of ice in North America, the MIS4 and LGM ice sheets are more zonally distributed along the Arctic coast (Fig. 7c,e). Hence, our simulations suggest that the North American ice sheet induces a westward migration of the Eurasian ice sheet, and consequently, the evolution of the Eurasian ice sheet between MIS4 and LGM was to a large extent controlled by the growth of the North American ice sheet.

The ice sheet's westward migration is depicted in Fig. 8, which shows the longitude of the center of mass (λ_c) of the total ice distribution in Eurasia. In the reconstructions from Kleman et al. (2013), λ_c decreases from 49°E at MIS5b to 44°E and 27°E at MIS4 and LGM, respectively (black bars in Fig. 8). Note that the westward migration between MIS4 and LGM is captured only if the North American ice sheet is present (white bars in Fig. 8), otherwise λ_c remains large ($\sim$55-60°E) for both stages (grey bars in Fig. 8).

4 Discussion

We have examined how the North American ice sheet (constrained by geological data) influences the extent of the Eurasian ice sheet in the MIS5b, MIS4 and LGM climate states. We found that the MIS4 and LGM ice sheets in North America yield a westward migration of the Eurasian ice sheet (Fig. 8), characterized by more ice in Europe and less ice in Siberia (Fig. 7). When accounting for the North American ice sheet, the spatial distributions of the simulated MIS4 and LGM ice sheets in Eurasia are in good agreement with contemporary proxy-based ice-sheet reconstructions (Fig. 7; Svendsen et al., 2004; Kleman et al., 2013); this suggests that the growth of the North American ice sheet between MIS4 and LGM may have been vital for limiting and shifting the Eurasian ice sheet westward in time.

4.1 North American influence on the Eurasian climate

The westward migration of the Eurasian ice sheet in the MIS4 and LGM simulations (Figs. 7 and 8) is associated with changes in the summer stationary wave field. The North American ice sheet yields a cooling (less ablation) in Europe and a warming (more ablation) in northeastern Siberia (Fig. 4f,h). These temperature anomalies are associated with an equivalent barotropic cyclonic/anticyclonic anomaly in the target regions (Fig. 6f,h).

The geopotential height anomalies in Fig. 6d,f,h result from (typically nonlinear) interactions between the atmospheric flow and the thermal and orographic forcing of the North American ice sheet. This leads to a complicated nonlinear response in the vicinity of the wave source (i.e. the North American ice sheet in our case) where the climate anomalies rotate clockwise for larger topographic barriers (Cook and Held, 1992; Ringler and Cook, 1997; Liakka et al., 2011; Liakka, 2012). Away from the wave source, however, the geopotential height anomalies share many similarities with linear wave theory (see Appendix A for details). For example, the low wavenumber polar wave train in Fig. 6d,f,h is consistent with a latitudinal decrease of the (barotropic) stationary wavenumber due to the spherical geometry of the planet (see Appendix A and Fig. 3 in the Supplement). In addition, linear Rossby ray tracing arguments (Appendix A and Hoskins and Karoly, 1981) suggest that higher latitude wave trains should have a more zonal orientation than at wave trains at lower latitudes, thus consistent with Fig. 6d,f,h.

Although the remote stationary wave response is broadly consistent with linear theory, our findings are different from the coupled ice sheet-climate model experiments in Beghin et al. (2014), who used CLIMBER-2 with (linear) parameterized stationary waves to examine the interaction between the Northern Hemisphere ice sheets. They found that the North American ice sheet has a negligible impact in European summer temperatures but yields a slight cooling in Siberia, thus contradicting our results (Fig. 4). Although CLIMBER has proven to be a valuable model for studying the transient ice sheet-climate evolution through the glacial cycles (e.g. Calov et al., 2002; Calov et al.,

2005; Bonelli et al., 2009; Ganopolski et al., 2010; Ganopolski and Calov, 2011), it has a very limited representation of the atmospheric circulation; in particular it does not account for Rossby wave dynamics. Unless explicitly corrected for (Ganopolski et al., 2010), the lack of Rossby wave dynamics in CLIMBER typically facilitates ice inception over the western rather than the eastern part of North America (Bonelli et al., 2009; Beghin et al., 2014); this presumably influenced the Eurasian climate anomalies in Beghin et al. (2014).

4.2 Sensitivity to OHT

Owing to the large uncertainty of the AMOC strength during glacial times (Otto-Bliesner et al., 2007; Weber et al., 2007), we perform sensitivity simulations of the equilibrium ice thickness using the atmospheric simulations with BO2009 OHT (Brandefelt and Otto-Bliesner, 2009) as climate forcing. The results are summarized in Fig. 9. Due to the colder conditions in the simulations with BO2009 OHT, the Eurasian ice sheet expands equatorward compared to when using PI OHT (cf. Fig. 9 and 7). However, despite the colder conditions in the North Atlantic, the model fails to simulate a large ice sheet at MIS5b (Fig. 9a,b).

Using the BO2009 OHT climate forcing, the North American ice sheet induces a westward migration of the Eurasian ice sheet (λ_c is reduced by 6° for MIS4 and by 11° for LGM; not shown); however, it is not as pronounced as with PI OHT (Fig. 8). Since the stationary wave response to the North American ice sheet is qualitatively similar in the BO2009 OHT (Figs. 4, 5 and 6 in the Supplement) and the PI OHT simulations (Figs. 4, 5 and 6), the reduced westward migration in the BO2009 OHT simulations is most likely attributed to the colder climate; in the PDD model, cold background conditions (temperatures below freezing) reduces the effect of temperature anomalies on the ablation.

4.3 What prevents ice-sheet growth at MIS5b?

The vexing issue of this study is that we fail to simulate a MIS5b ice sheet of comparable size to the data-based reconstructions (Figs. 7 and 9). The lack of ice growth at MIS5b is associated with a negative surface mass balance across the entire Eurasian continent (Fig. 2 in the Supplement) due to relatively high summer temperatures (Fig. 4 and Table 2). The relatively warm conditions at MIS5b compared to MIS4 and LGM are attributed both to a higher insolation and higher concentrations of greenhouse gases (Table 1). It is possible that allowing for certain feedbacks, such as vegetation changes (Colleoni et al., 2009; Liakka et al., 2014), would cool the summer climate and thus support ice inception at MIS5b. However, since the MIS4 and LGM extents of the Eurasian ice sheet are in good agreement with the reconstructions when omitting these feedbacks, it seems unlikely that systematic biases in the climate forcing is the primary cause for the lack of ice growth at MIS5b.

In addition, we fail to find multiple equilibrium states (e.g. Calov and Ganopolski, 2005; Abe-Ouchi et al., 2013) of the simulated Eurasian ice sheets (Fig. 7 in the Supplement); initializing the

ice-sheet simulations using the Kleman et al. (2013) reconstructions leads to very similar equilibrium extents as in Fig. 7. This suggests that preceding configurations of the Eurasian ice sheet were not crucial for maintaining the ice sheet at MIS5b.

Instead, it is more likely that the MIS5b ice sheet was not in equilibrium with the prevailing climate. The successful glacial inception and good agreement between the equilibrated MIS4 and LGM ice sheets and the reconstructions suggests that the climate was locally cold enough to support glacial inception and the resulting ice sheets were in equilibrium with the prevailing climate; this is, however, not necessarily true for MIS5b. Instead, it is plausible that the MIS5b climate was too warm to support glacial inception and the ice sheet was a remnant of ice growth in preceding colder periods. In this context it is interesting to note that the Eurasian ice sheet reached a size comparable to MIS5b already at $\sim$105 kyrs BP, subsequent to a relative minimum in the high-latitude boreal summer insolation (Kleman et al., 2013; Löfverström et al., 2014).

Since we do not have access to any atmospheric simulations of a colder stages prior to MIS5b, we use a crude approach by imposing a cooling of the JJA temperature artificially in SICOPOLIS. To estimate the magnitude of the cooling, we employ the parameterization of the surface temperature to changing insolation proposed by Abe-Ouchi et al. (2007, 2013); based on sensitivity experiments with a coupled atmosphere-ocean model, they obtained a linear relationship between changes of the high-latitude temperature (ΔT_{insol}) and insolation (ΔQ): $\Delta T_{insol} = 3.25 \times \Delta Q/40$. The insolation at the youngest minimum preceding 88 kyrs BP (at $\sim$95 kyrs BP) was about 40 W m^{-2} lower than at 88 kyrs BP (Berger and Loutre, 1991); this yields $\Delta T_{insol} \approx -3^{\circ}$C. Using the colder "minimum insolation" conditions, the extent of the Eurasian ice sheet agrees well with the MIS5b reconstruction in Scandinavia and the Barents sea region (Fig. 10) – in particular when the North American ice sheet is included (Fig. 10b) – whereas the Kara sea region continually remains ice free. Hence, in contrast to MIS4 and LGM, our first-order sensitivity analysis suggests that the MIS5b extent of the Eurasian ice sheet results as a memory of preceding colder stages rather than the prevailing climate.

5 Conclusions

We have examined the impact of the geologically-constrained MIS5b, MIS4 and LGM ice sheets in North America on the spatial extent of the Eurasian ice sheet. The conclusions are summarized as follows:

- The North American ice sheet yields cooler summer temperatures in Europe and warmer temperatures in northeastern Siberia in all time slices. The amplitude of these anomalies and the westward extent of the Siberian warming increase with the size of the North American ice sheet (Fig. 4).

- The temperature anomalies are associated with an equivalent barotropic cyclonic and anticyclonic anomaly in Europe and Siberia, respectively (Fig. 6). The structure of the circulation

anomalies away from the wave forcing is qualitatively consistent with linear barotropic stationary wave theory (see Appendix A).

– Owing to its impact on the Eurasian summer temperatures, the North American ice sheet controls the westward migration of the Eurasian ice sheet; in the presence of the North American ice sheet, the spatial extents of the simulated Eurasian ice sheets at MIS4 and LGM are consistent with contemporary ice-sheet reconstructions (Svendsen et al., 2004; Kleman et al., 2013). However, if the North American ice sheet is omitted, the Eurasian ice sheet becomes more zonally distributed with a more eastward located center of mass (Figs. 7, 8).

– The stationary wave response to the North American glacial topography is not that sensitive to changes in the ocean heat transport (compare Figs. 4 and 6 with Figs. 4 and 6 in the Supplement). Nevertheless, a weakening of AMOC reduces the influence of the North American glacial topography on the Eurasian ice-sheet evolution by imposing cooler background conditions in Eurasia (Fig. 9).

– Although the spatial extents of the MIS4 and LGM ice sheets are well captured by SICOPOLIS, Eurasia remains essentially ice free for MIS5b. Unlike MIS4 and LGM, first-order sensitivity analysis reveals that the MIS5b ice sheet was not in equilibrium with the prevailing climate, but more likely a result of preceding colder climate conditions.

– Our study suggests that the westward migration of the Eurasian ice sheet between MIS4 and LGM was induced by the expansion of the North American ice sheet. Furthermore, our results are consistent with the notion that the east-heavy Eurasian ice sheet at the late Saalian Maximum ($\sim$140 kyrs BP) was accompanied by a relatively small ice sheet in North America (Svendsen et al., 2004; Colleoni et al., 2014).

Appendix A

Due to the complexity of the atmospheric model it is useful to resort to a simpler linear framework to obtain a conceptual understanding of the stationary wave field. Linear models have been shown to qualitatively capture the large-scale features of the stationary waves in the present-day atmosphere (Charney and Eliassen, 1949; Held, 1983; Held et al., 2002). However, many features omitted in linear models (e.g. zonal variations in the background state and nonlinear interactions between different forcing agents) can significantly alter the stationary wave response (e.g. Cook and Held, 1992; Hoskins and Ambrizzi, 1993; Ringler and Cook, 1997). Therefore, results from linear models should only be considered as a qualitative first-order estimate of the total wave response. The equivalent barotropic structure in Fig. 6d,f,h suggests that the wave field is dominated by orographic rather than thermal forcing; the latter has been shown to yield stationary waves with a more baroclinic structure (geopotential height anomalies tilt westward with altitude Hoskins and Karoly, 1981; Ting, 1994;

Ringler and Cook, 1999). Therefore, we use the orographically forced linear barotropic model (this is the simplest model that can be used to study meridional dispersion of stationary waves; Held, 1983).

In models linearized about a zonal mean basic state, the horizontal scale of the stationary waves is given by the "stationary wavenumber" K_s, which is a function of the atmospheric background state. In a barotropic model, K_s is given by (Held, 1983):

$$K_s^2 = k^2 + l^2 = \cos^2\phi \left(\frac{\beta + a^{-1}\partial[\zeta]/\partial\phi}{[u]} \right), \tag{A1}$$

where β and $a^{-1}\partial[\zeta]/\partial\phi$ are the meridional gradients of planetary and (zonal mean) relative vorticity, $[u]$ is the zonal mean background flow, ϕ the latitude and k and l denote zonal and meridional wavenumbers, respectively. In the present-day atmosphere (Hoskins and Karoly, 1981; Held, 1983) as well as in our simulations (Fig. 3 in the Supplement), K_s is monotonically decreasing with latitude (as $\beta \sim cos(\phi) \to 0$ toward the pole). This implies that stationary waves at high latitudes typically have lower zonal wavenumbers than those propagating at lower latitudes. Hence, the low wavenumber response (small K_s) at high latitudes in Fig. 6d,f,h ($> 60°$N) is essentially a result of the spherical geometry of the planet.

Following Hoskins and Karoly (1981), the propagation direction of stationary waves is given by the direction of the local group velocity (in the limit of WKB): $\mathbf{c_g} = (c_{gx}\mathbf{i}, c_{gy}\mathbf{j})$, where $\mathbf{i}$ and $\mathbf{j}$ are the unit vectors in the zonal and meridional direction, respectively. Because c_{gy} is identical to c_{gx} except for a factor l instead of k (Hoskins and Karoly, 1981; Vallis, 2006)[2] , the inclination (α) of the ray path (propagation direction) is given by:

$$\tan\alpha = \frac{c_{gy}}{c_{gx}} = \frac{l}{k}. \tag{A2}$$

Here, k is constant along a ray; hence as K_s decreases with latitude (Fig. 3 in the Supplement), $|l|$ must decrease to satisfy Eq. A1. This implies that waves at high latitudes propagate along more zonal paths than waves at lower latitudes (Eq. A2); this is also seen in Fig. 6d,f,h, where the polar wave train is more zonally oriented than the subtropical wave train. Hence, despite the high complexity of the atmospheric circulation model used here, the key features (wavenumber and orientation) of the polar wave train in Fig. 6d,f,h – that are associated with the westward migration of the Eurasian ice sheet – are consistent with linear barotropic theory.

Acknowledgements. We are grateful to Prof. Johan Kleman for providing the ice-sheet reconstructions. We acknowledge support from the research funding programme "LOEWE-Landesoffensive zur Entwicklung Wissenschaftlich-ökonomischer Exzellenz" of Hesse's Ministry of Higher Education. The LOEWE initiative also provided finan-

[2]For stationary waves, $c_{gx} = 2\beta k^2/(k^2+l^2)^2$ and $c_{gy} = 2\beta kl/(k^2+l^2)^2$. Hence, $c_{gx} > 0$, which implies that the wave energy always propagates eastward. c_{gy}, on the other hand, depends on the sign of l, which corresponds to poleward (positive l) and equatorward (negative l) propagation.

cial support for the simulations, which were carried out at the LOEWE Frankfurt Centre for Scientific Computing (LOEWE-CSC). We thank two anonymous reviewers for insightful comments on the manuscript.

References

Abe-Ouchi, A., Segawa, T., and Saito, F.: Climatic conditions for modelling the Northern Hemisphere ice sheets throughout the ice age cycle, Climate of the Past, 3, 423–438, 2007.

Abe-Ouchi, A., Saito, F., Kawamura, K., Raymo, M. E., Okuno, J., Takahashi, K., and Blatter, H.: Insolation-driven 100,000-year glacial cycles and hysteresis of ice-sheet volume, Nature, 500, 190–193, 2013.

Beghin, P., Charbit, S., Dumas, C., Kageyama, M., Roche, D., and Ritz, C.: Interdependence of the growth of the Northern Hemisphere ice sheets during the last glaciation: the role of atmospheric circulation, Climate of the Past, 10, 345–358, 2014.

Berger, A. and Loutre, M.-F.: Insolation values for the climate of the last 10 million years, Quaternary Science Reviews, 10, 297–317, 1991.

Bitz, C., Holland, M., Hunke, E., and Moritz, R.: Maintenance of the sea-ice edge, Journal of climate, 18, 2903–2921, 2005.

Bitz, C. M., Shell, K., Gent, P., Bailey, D., Danabasoglu, G., Armour, K., Holland, M., and Kiehl, J.: Climate sensitivity of the community climate system model, version 4, Journal of Climate, 25, 3053–3070, 2012.

Bonelli, S., Charbit, S., Kageyama, M., Woillez, M.-N., Ramstein, G., Dumas, C., and Quiquet, A.: Investigating the evolution of major Northern Hemisphere ice sheets during the last glacial-interglacial cycle, Climate of the Past, 5, 1013–1053, 2009.

Bradwell, T., Stoker, M. S., Golledge, N. R., Wilson, C. K., Merritt, J. W., Long, D., Everest, J. D., Hestvik, O. B., Stevenson, A. G., Hubbard, A. L., et al.: The northern sector of the last British Ice Sheet: maximum extent and demise, Earth-Science Reviews, 88, 207–226, 2008.

Brady, E. C., Otto-Bliesner, B. L., Kay, J. E., and Rosenbloom, N.: Sensitivity to glacial forcing in the CCSM4, Journal of Climate, 26, 1901–1925, 2013.

Braithwaite, R. J. and Olesen, O. B.: Calculation of glacier ablation from air temperature, West Greenland, in: Glacier fluctuation and climate change, edited by Oerlemans, J., pp. 219–233, Kluwer, Dordrecht, 1989.

Brandefelt, J. and Otto-Bliesner, B. L.: Equilibration and variability in a Last Glacial Maximum climate simulation with CCSM3, Geophys. Res. Lett., 36, L19712, doi:10.1029/2009GL040364, 2009.

Calov, R. and Ganopolski, A.: Multistability and hysteresis in the climate-cryosphere system under orbital forcing, Geophysical research letters, 32, 2005.

Calov, R. and Greve, R.: A semi-analytical solution for the positive degree-day model with stochastic temperature variations, Journal of Glaciology, 51, 173–175, 2005.

Calov, R., Ganopolski, A., Petoukhov, V., Claussen, M., and Greve, R.: Large-scale instabilities of the Laurentide ice sheet simulated in a fully coupled climate-system model, Geophysical Research Letters, 29, 2002.

Calov, R., Ganopolski, A., Petoukhov, V., Claussen, M., Brovkin, V., and Kubatzki, C.: Transient simulation of the last glacial inception. Part II: sensitivity and feedback analysis, Clim. Dyn., 24, 563–576, 2005.

Charbit, S., Ritz, C., and Ramstein, G.: Simulations of Northern Hemisphere ice-sheet retreat:. sensitivity to physical mechanisms involved during the Last Deglaciation, Quaternary Science Reviews, 21, 243–265, doi:10.1016/S0277-3791(01)00093-2, 2002.

Charbit, S., Ritz, C., Philippon, G., Peyaud, V., and Kageyama, M.: Numerical reconstructions of the Northern Hemisphere ice sheets through the last glacial-interglacial cycle, Climate of the Past, 3, 15–37, 2007.

Charney, J. G. and Eliassen, A.: A numerical method for predicting the perturbations of the middle latitude westerlies, Tellus A, 1, 1949.

Clark, P., Clague, J., Curry, B., Dreimanis, A., Hicock, S., Miller, G., Berger, G., Eyles, N., Lamothe, M., Miller, B., et al.: Initiation and development of the Laurentide and Cordilleran ice sheets following the last interglaciation, Quaternary Science Reviews, 12, 79–114, 1993.

Colleoni, F., Krinner, G., and Jakobsson, M.: Sensitivity of the Late Saalian (140 kyrs BP) and LGM (21 kyrs BP) Eurasian ice sheet surface mass balance to vegetation feedbacks, Geophys. Res. Lett., 36, doi:10.1029/2009GL037200, 2009.

Colleoni, F., Wekerle, C., and Masina, S.: Long-term safety of a planned geological repository for spent nuclear fuel in Forsmark - estimate of maximum ice sheet thicknesses, Technical Report SKB TR-14-21, SKB, 2014.

Collins, W. D., Rasch, P. J., Boville, B. A., Hack, J. J., McCaa, J. R., Williamson, D. L., Kiehl, J. T., Briegleb, B., Bitz, C., Lin, S., et al.: Description of the NCAR community atmosphere model (CAM 3.0), Tech. Note NCAR/TN-464+ STR, NCAR, 2004.

Collins, W. D. et al.: The formulation and atmospheric simulation of the Community Atmosphere Model: CAM3, J. Clim., 19, 2144–2161, 2006.

Cook, K. H. and Held, I. M.: Stationary waves of the ice age climate, Journal of climate, 1, 807–819, 1988.

Cook, K. H. and Held, I. M.: The stationary response to large-scale orography in a general circulation model and a linear model, Journal of the atmospheric sciences, 49, 525–539, 1992.

De Vernal, A., Eynaud, F., Henry, M., Hillaire-Marcel, C., Londeix, L., Mangin, S., Matthießen, J., Marret, F., Radi, T., Rochon, A., et al.: Reconstruction of sea-surface conditions at middle to high latitudes of the Northern Hemisphere during the Last Glacial Maximum (LGM) based on dinoflagellate cyst assemblages, Quaternary Science Reviews, 24, 897–924, 2005.

De Vernal, A., Rosell-Melé, A., Kucera, M., Hillaire-Marcel, C., Eynaud, F., Weinelt, M., Dokken, T., and Kageyama, M.: Comparing proxies for the reconstruction of LGM sea-surface conditions in the northern North Atlantic, Quaternary Science Reviews, 25, 2820–2834, 2006.

Dee, D. P., Uppala, S. M., Simmons, A. J., Berrisford, P., Poli, P., Kobayashi, S., Andrae, U., Balmaseda, M. A., Balsamo, G., Bauer, P., Bechtold, P., Beljaars, A. C. M., van de Berg, L., Bidlot, J., Bormann, N., Delsol, C., Dragani, R., Fuentes, M., Geer, A. J., Haimberger, L., Healy, S. B., Hersbach, H., Hólm, E. V., Isaksen, L., Kållberg, P., Köhler, M., Matricardi, M., McNally, A. P., Monge-Sanz, B. M., Morcrette, J.-J., Park, B.-K., Peubey, C., de Rosnay, P., Tavolato, C., Thépaut, J.-N., and Vitart, F.: The ERA-Interim reanalysis: configuration and performance of the data assimilation system, Quart. J. Roy. Meteor. Soc., 137, 553–597, 2011.

Ganopolski, A. and Calov, R.: The role of orbital forcing, carbon dioxide and regolith in 100 kyr glacial cycles, Climate of the Past, 7, 1415–1425, 2011.

Ganopolski, A., Calov, R., and Claussen, M.: Simulation of the last glacial cycle with a coupled climate ice-sheet model of intermediate complexity, Climate of the Past, 6, 229–244, 2010.

Greve, R.: Application of a Polythermal Three-Dimensional Ice Sheet Model to the Greenland Ice Sheet: Response to Steady-State and Transient Climate Scenarios., J. Clim., 10, 901–918, 1997.

Held, I. M.: Stationary and quasi-stationary eddies in the extratropical troposphere: Theory, Large-scale dynamical processes in the atmosphere, pp. 127–168, 1983.

Held, I. M., Ting, M., and Wang, H.: Northern winter stationary waves: theory and modeling, Journal of Climate, 15, 2125–2144, 2002.

Hoskins, B. J. and Ambrizzi, T.: Rossby wave propagation on a realistic longitudinally varying flow, Journal of the Atmospheric Sciences, 50, 1661–1671, 1993.

Hoskins, B. J. and Karoly, D. J.: The steady linear response of a spherical atmosphere to thermal and orographic forcing, Journal of the Atmospheric Sciences, 38, 1179–1196, 1981.

Hurrell, J. W., Hack, J. J., Phillips, A. S., Caron, J., and Yin, J.: The dynamical simulation of the Community Atmosphere Model version 3 (CAM3), Journal of climate, 19, 2162–2183, 2006.

Hutter, K.: Theoretical glaciology: material science of ice and the mechanics of glaciers and ice sheets, Reidel, Dordrecht, 1983.

Kageyama, M., Braconnot, P., Bopp, L., Caubel, A., Foujols, M.-A., Guilyardi, E., Khodri, M., Lloyd, J., Lombard, F., Mariotti, V., et al.: Mid-Holocene and Last Glacial Maximum climate simulations with the IPSL model—part I: comparing IPSL_CM5A to IPSL_CM4, Climate dynamics, 40, 2447–2468, 2013.

Kaspi, Y. and Schneider, T.: Winter cold of eastern continental boundaries induced by warm ocean waters, 2011.

Kleman, J., Jansson, K., De Angelis, H., Stroeven, A. P., Hättestrand, C., Alm, G., and Glasser, N.: North American ice sheet build-up during the last glacial cycle, 115–21kyr, Quaternary Science Reviews, 29, 2036–2051, 2010.

Kleman, J., Fastook, J., Ebert, K., Nilsson, J., and Caballero, R.: Pre-LGM Northern Hemisphere ice sheet topography, Climate of the Past, 9, 2365–2378, doi:10.5194/cp-9-2365-2013, 2013.

Li, C. and Battisti, D.: Reduced Atlantic Storminess during Last Glacial Maximum: Evidence from a Coupled Climate Model, Journal of Climate, 21, 3561–3579, 2008.

Liakka, J.: Interactions between topographically and thermally forced stationary waves: implications for ice-sheet evolution, Tellus A, 64, 2012.

Liakka, J. and Nilsson, J.: The impact of topographically forced stationary waves on local ice-sheet climate, Journal of Glaciology, 56, 534–544, 2010.

Liakka, J., Nilsson, J., and Löfverström, M.: Interactions between stationary waves and ice sheets: linear versus nonlinear atmospheric response, Clim. Dyn., 38, 1249–1262, 2011.

Liakka, J., Colleoni, F., Ahrens, B., and Hickler, T.: The impact of climate-vegetation interactions on the onset of the Antarctic ice sheet, Geophysical Research Letters, 41, 1269–1276, 2014.

Löfverström, M., Caballero, R., Nilsson, J., and Kleman, J.: Evolution of the large-scale atmospheric circulation in response to changing ice sheets over the last glacial cycle, Climate of the Past, 10, 1453–1471, doi:10.5194/cp-10-1453-2014, 2014.

Löfverström, M., Liakka, J., and Kleman, J.: The North American Cordillera - an impediment to growing the continent-wide Laurentide Ice Sheet, J. Climate, doi:10.1175/JCLI-D-15-0044.1, 2015.

Margo Project Members, Waelbroeck, C., Paul, A., Kucera, M., Rosell-Melé, A., Weinelt, M., Schneider, R., Mix, A. C., Abelmann, A., Armand, L., Bard, E., Barker, S., Barrows, T. T., Benway, H., Cacho, I., Chen, M.-T., Cortijo, E., Crosta, X., de Vernal, A., Dokken, T., Duprat, J., Elderfield, H., Eynaud, F., Gersonde, R., Hayes, A., Henry, M., Hillaire-Marcel, C., Huang, C.-C., Jansen, E., Juggins, S., Kallel, N., Kiefer, T., Kienast, M., Labeyrie, L., Leclaire, H., Londeix, L., Mangin, S., Matthiessen, J., Marret, F., Meland, M., Morey, A. E., Mulitza, S., Pflaumann, U., Pisias, N. G., Radi, T., Rochon, A., Rohling, E. J., Sbaffi, L., Schäfer-Neth,

C., Solignac, S., Spero, H., Tachikawa, K., and Turon, J.-L.: Constraints on the magnitude and patterns of ocean cooling at the Last Glacial Maximum, Nature Geoscience, 2, 127–132, doi:10.1038/ngeo411, 2009.

Marshall, S. J., Tarasov, L., Clarke, G. K., and Peltier, W. R.: Glaciological reconstruction of the Laurentide Ice Sheet: physical processes and modelling challenges, Canadian Journal of Earth Sciences, 37, 769–793, 2000.

Marsiat, I.: Simulation of the Northern Hemisphere continental ice sheets over the last glacial-interglacial cycle: experiments with a latitude-longitude vertically integrated ice sheet model coupled to a zonally averaged climate model, Paleoclimates, 1, 59–98, 1994.

Merz, N., Raible, C. C., and Woollings, T.: North Atlantic eddy-driven jet in interglacial and glacial winter climates, Journal of Climate, 28, 3977–3997, 2015.

Oleson, K. et al.: Technical Description of the Community Land Model (CLM), NCAR Tech. Note NCAR/TN-461+STR, Natl. Cent. for Atmos. Res., Boulder, Colo., 2004.

Otto-Bliesner, B., Hewitt, C., Marchitto, T., Brady, E., Abe-Ouchi, A., Crucifix, M., Murakami, S., and Weber, S.: Last Glacial Maximum ocean thermohaline circulation: PMIP2 model intercomparisons and data constraints, Geophysical Research Letters, 34, 2007.

Otto-Bliesner, B. L., Brady, E. C., Clauzet, G., Tomas, R., Levis, S., and Kothavala, Z.: Last glacial maximum and Holocene climate in CCSM3, Journal of Climate, 19, 2526–2544, 2006.

Paul, A. and Schäfer-Neth, C.: Modeling the water masses of the Atlantic Ocean at the Last Glacial Maximum, Paleoceanography, 18, 1058, doi:10.1029/2002PA000783, 2003.

Pausata, F. S. and Löfverström, M.: On the enigmatic similarity in Greenland δ18O between the Oldest and Younger Dryas, Geophysical Research Letters, 42, 2015.

Peltier, W. and Fairbanks, R. G.: Global glacial ice volume and Last Glacial Maximum duration from an extended Barbados sea level record, Quaternary Science Reviews, 25, 3322–3337, 2006.

Petit, J. R., Jouzel, J., Raynaud, D., Barkov, N. I., Barnola, J.-M., Basile, I., Bender, M., Chappellaz, J., Davis, M., Delaygue, G., Delmotte, M., Kotlyakov, V. M., Legrand, M., Lipenkov, V. Y., Lorius, C., Pépin, L., Ritz, C., Saltzman, E., and Stievenard, M.: Climate and atmospheric history of the past 420,000 years from the Vostok ice core, Antarctica, Nature, 399, 429–436, doi:10.1038/20859, 1999.

Reeh, N.: Parameterization of melt rate and surface temperature on the Greenland ice sheet, Polarforschung, 59, 113–128, 1991.

Ringler, T. D. and Cook, K. H.: Factors controlling nonlinearity in mechanically forced stationary waves over orography, Journal of the atmospheric sciences, 54, 2612–2629, 1997.

Ringler, T. D. and Cook, K. H.: Understanding the seasonality of orographically forced stationary waves: Interaction between mechanical and thermal forcing, Journal of the atmospheric sciences, 56, 1154–1174, 1999.

Roe, G. H.: Orographic precipitation, Annu. Rev. Earth Planet. Sci., 33, 645–671, 2005.

Roe, G. H. and Lindzen, R. S.: The Mutual Interaction between Continental-Scale Ice Sheets and Atmospheric Stationary Waves., Journal of Climate, 14, 1450–1465, doi:10.1175/1520-0442(2001)014<1450:TMIBCS>2.0.CO;2, 2001.

Sanberg, J. and Oerlemans, J.: Modelling of Pleistocene European ice sheets: the effect of upslope precipitation, Geologie en Mijnbouw, 62, 267–273, 1983.

Smith, L. M., Miller, G. H., Otto-Bliesner, B., and Shin, S.-I.: Sensitivity of the Northern Hemisphere climate system to extreme changes in Holocene Arctic sea ice, Quaternary Science Reviews, 22, 645–658, 2003.

Spahni, R., Chappellaz, J., Stocker, T. F., Loulergue, L., Hausammann, G., Kawamura, K., Flückiger, J., Schwander, J., Raynaud, D., Masson-Delmotte, V., and Jouzel, J.: Atmospheric Methane and Nitrous Oxide of the Late Pleistocene from Antarctic Ice Cores, Science, 310, 1317–1321, doi:10.1126/science.1120132, 2005.

Stokes, C. R., Tarasov, L., and Dyke, A. S.: Dynamics of the North American Ice Sheet Complex during its inception and build-up to the Last Glacial Maximum, Quaternary Science Reviews, 50, 86–104, 2012.

Svendsen, J. I., Alexanderson, H., Astakhov, V. I., Demidov, I., Dowdeswell, J. A., Funder, S., Gataullin, V., Henriksen, M., Hjort, C., Houmark-Nielsen, M., et al.: Late Quaternary ice sheet history of northern Eurasia, Quaternary Science Reviews, 23, 1229–1271, 2004.

Ting, M.: Maintenance of northern summer stationary waves in a GCM, Journal of the atmospheric sciences, 51, 3286–3308, 1994.

Toracinta, E. R., Oglesby, R. J., and Bromwich, D. H.: Atmospheric Response to Modified CLIMAP Ocean Boundary Conditions during the Last Glacial Maximum(., Journal of Climate, 17, 504–522, 2004.

Ullman, D., LeGrande, A., Carlson, A., Anslow, F., and Licciardi, J.: Assessing the impact of Laurentide Ice Sheet topography on glacial climate, Climate of the Past, 10, 487–507, 2014.

Vallis, G. K.: Atmospheric and oceanic fluid dynamics: fundamentals and large-scale circulation, Cambridge University Press, 2006.

Van Den Berg, J., van de Wal, R., and Oerlemans, H.: A mass balance model for the Eurasian Ice Sheet for the last 120,000 years, Global and Planetary Change, 61, 194–208, 2008.

Van der Veen, C. J.: Fundamentals of glacier dynamics, CRC Press, 2013.

Weber, S., Drijfhout, S., Abe-Ouchi, A., Crucifix, M., Eby, M., Ganopolski, A., Murakami, S., Otto-Bliesner, B., and Peltier, W.: The modern and glacial overturning circulation in the Atlantic ocean in PMIP coupled model simulations, Climate of the Past, 3, 51–64, 2007.

Weertman, J.: The theory of glacier sliding, Journal of Glaciology, 5, 287–303, 1964.

Zweck, C. and Huybrechts, P.: Modeling of the northern hemisphere ice sheets during the last glacial cycle and glaciological sensitivity, Journal of Geophysical Research: Atmospheres (1984–2012), 110, 2005.

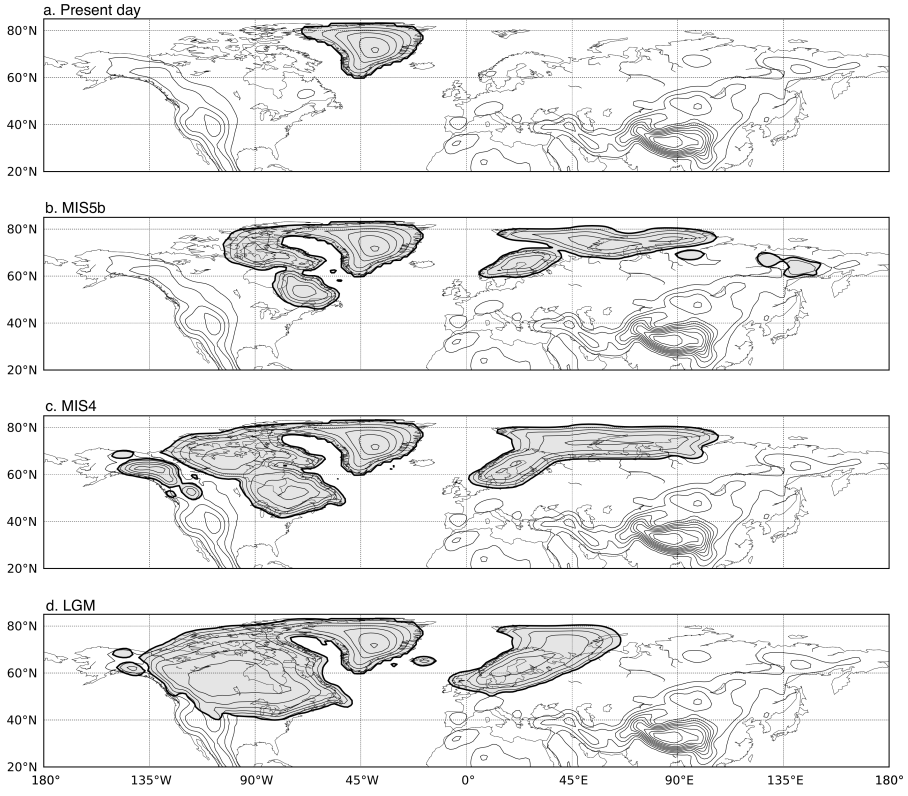

Figure 1. Northern Hemisphere topography representative for (a) present-day and PI, (b) MIS5b, (c) MIS4 and (d) LGM, based on the ice-sheet reconstructions in Kleman et al. (2013). The shading represents ice sheets and the contour interval is 500 m.

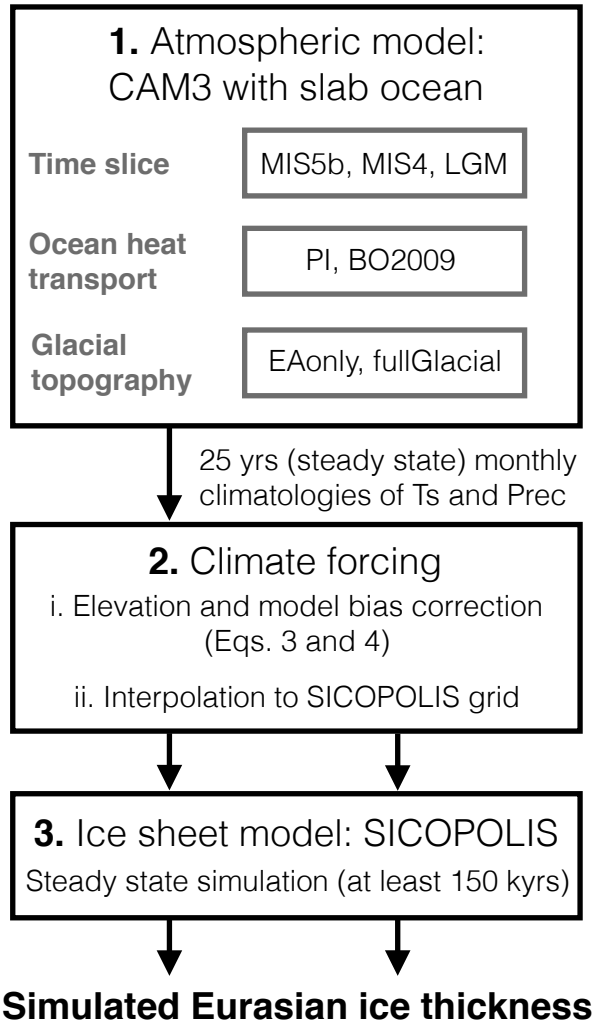

Figure 2. Schematic flow diagram (from top to bottom) of the experimental setup. Step 1: three glacial time slice experiments are carried out with the atmospheric model, using two different representation of ocean heat transport and glacial topography. Step 2: monthly climatologies of surface temperature (Ts) and precipitation (Prec) are used create the climate forcing fields which are interpolated to the ice-sheet model grid. Step 3: steady-state ice-sheet model simulations are carried out to obtain the ice thickness in Eurasia. A more detailed description of the experimental setup is provided in the main text.

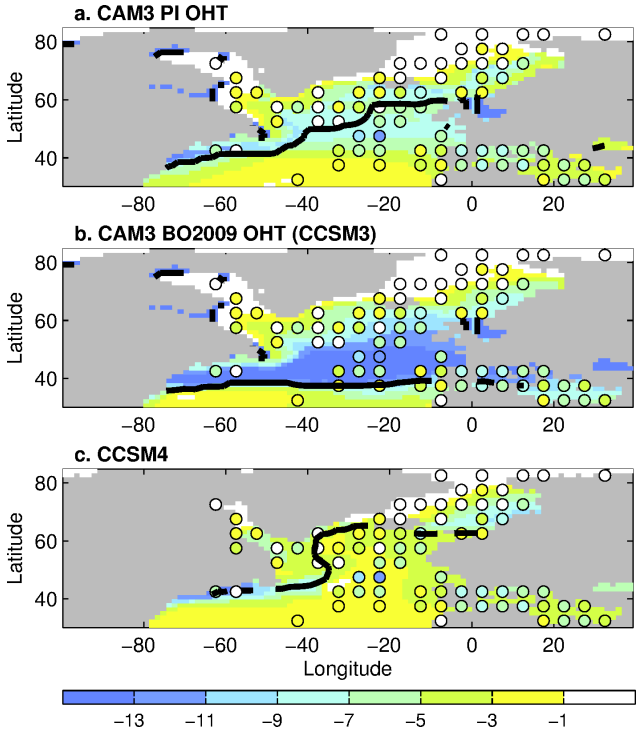

Figure 3. The colored shading illustrates the simulated annual mean SST anomalies (LGM-PI; in °C) in the North Atlantic from the CAM3 simulations using (a) PI OHT and (b) BO2009 OHT (Brandefelt and Otto-Bliesner, 2009) as well as (c) the LGM simulation from Brady et al. (2013) using the Community Climate System Model version 4 (CCSM4). The equatorward location of the annual-mean sea-ice margin in the respective LGM simulation is depicted by the thick black contours in each panel. The colored markers in each panel show the (annual mean) LGM SST anomaly (LGM-PI) from the MARGO SST reconstruction (Margo Project Members et al., 2009).

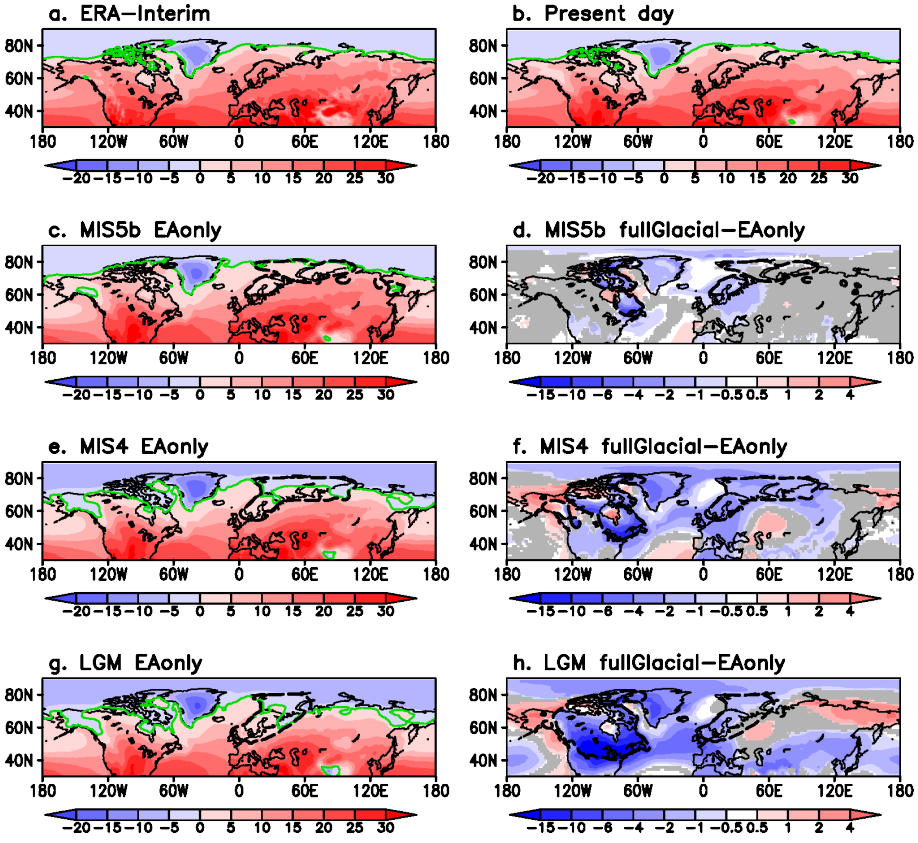

Figure 4. Boreal summer (JJA) surface temperature (in °C) from (a) the ERA-Interim climatology (Dee et al., 2011), (b) the present-day simulation, and the EAonly simulations (with PI OHT) of (c) MIS5b, (e) MIS4 and (g) LGM; green contour denotes the zero-degree surface isotherm. Panels d,f,h show the JJA surface temperature anomalies induced by the North American ice sheet (the difference between the fullGlacial and EAonly simulations; in °C) for (d) MIS5b, (f) MIS4 and (h) LGM. The temperature in the glacial simulations (c to h) has been projected to the present-day orography using the standard lapse rate ($\gamma = -6.5 \times 10^{-3}$ K m^{-1}). The dashed black contours depict the outlines of the Kleman et al. (2013) ice-sheet reconstructions in Eurasia and North America. Only significant changes at 95% (based on Student?s t-test) are shown in d,f,h (non-significant changes are displayed in gray).

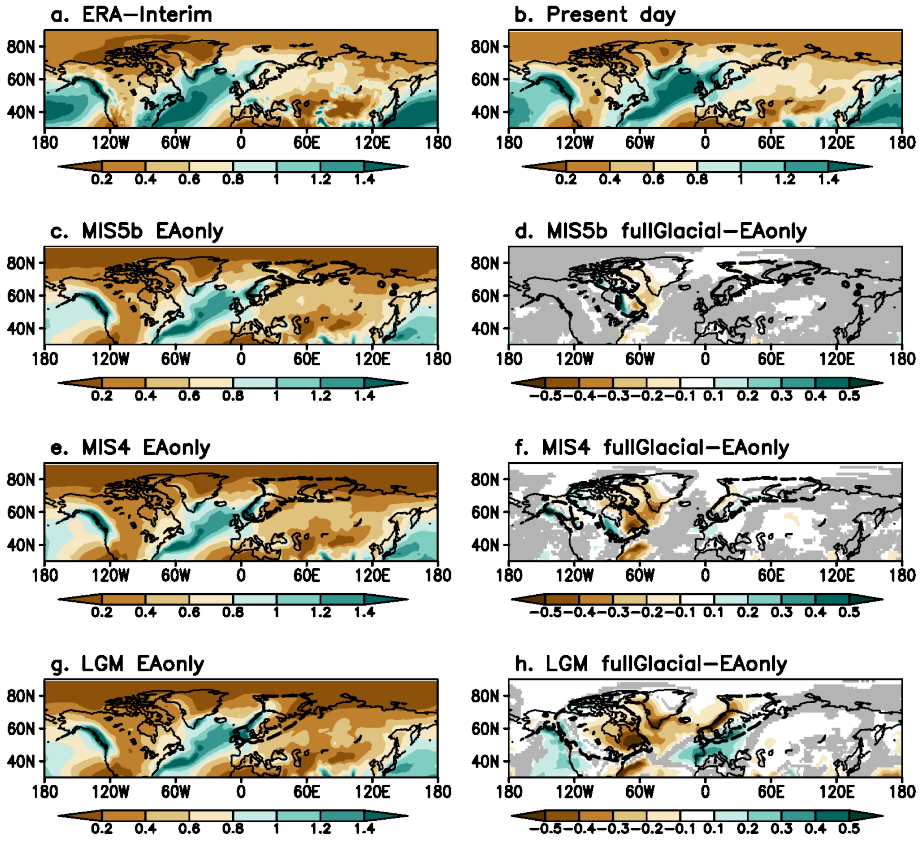

Figure 5. Annual precipitation (in m) from (a) the ERA-Interim climatology (Dee et al., 2011), (b) the present-day simulation, and the EAonly simulations (with PI OHT) of (c) MIS5b, (e) MIS4 and (g) LGM. The annual precipitation anomalies induced by North American ice sheet (the difference between the fullGlacial and EAonly simulations; in m) are shown in (d,f,h) for (d) MIS5b, (f) MIS4 and (h) LGM. The dashed black contours depict the outlines of the Kleman et al. (2013) ice-sheet reconstructions in Eurasia and North America. Only significant changes at 95% (based on Student?s t-test) are shown in d,f,h (non-significant changes are displayed in gray).

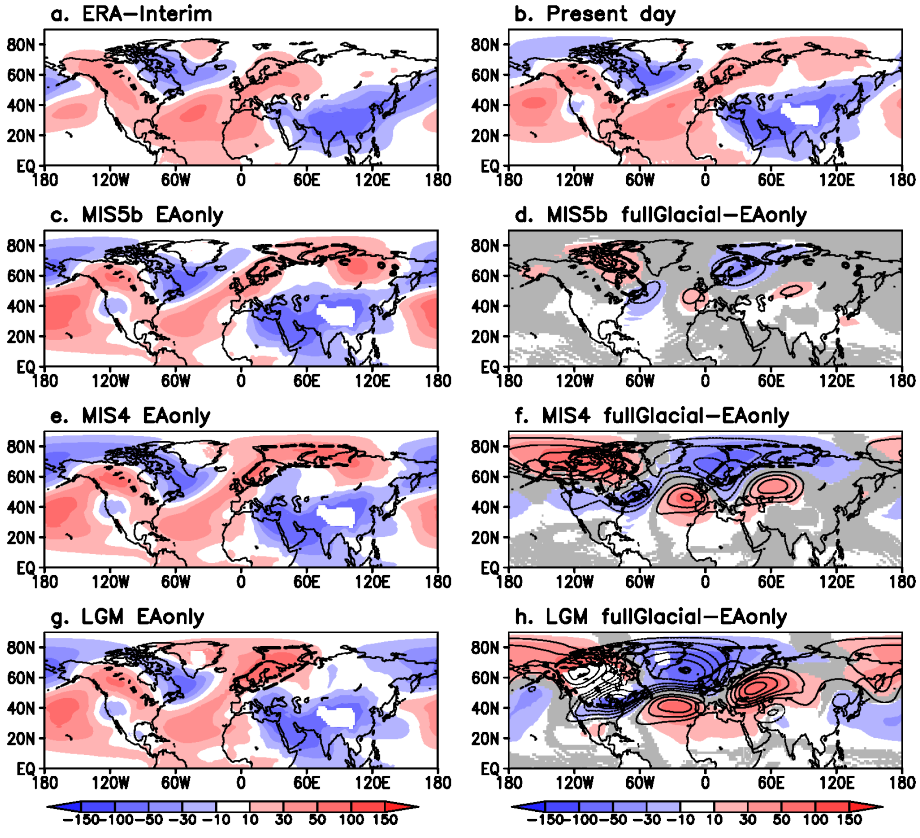

Figure 6. Same as Fig. 5 but for the JJA geopotential height anomalies (in m; zonal mean subtracted) at 700 hPa (shading) and 300 hPa (black contours in d,f,h; contour interval is 30 m, and negative values are dashed). Positive anomalies refer to a anticyclonic circulation anomaly, and negative anomalies to a cyclonic circulation anomaly. Only significant changes at 95% (based on Student?s t-test) are shown in d,f,h (non-significant changes are displayed in gray).

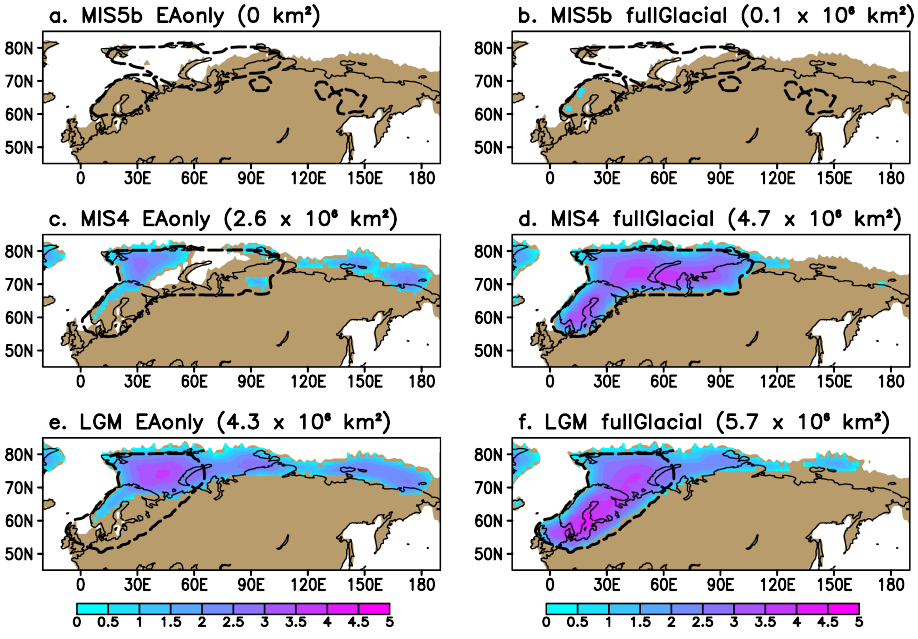

Figure 7. Simulated equilibrium ice thickness in Eurasia (shading; in km) using the PI OHT climate forcing from the EAonly (a,c,e) and fullGlacial (b,d,f) simulations for MIS5b (a,b), MIS4 (c,d) and LGM (e,f). The dashed black contours depict the outlines of the Kleman et al. (2013) ice-sheet reconstructions. The land area in the simulations is indicated by the brown color, and the present-day coastline by the thin black contour. The total Eurasian ice-sheet area in each simulation is indicated in the panel titles.

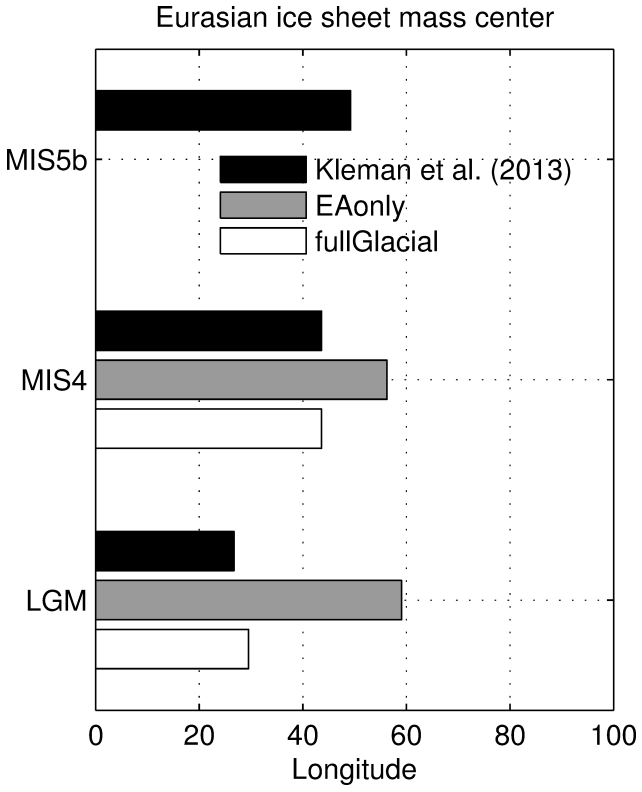

Figure 8. The longitude of the center of mass of the total ice distribution in Eurasia (λ_c) in the Kleman et al. (2013) reconstructions (black bars), EAonly simulations (gray bars), and fullGlacial simulations (white bars).

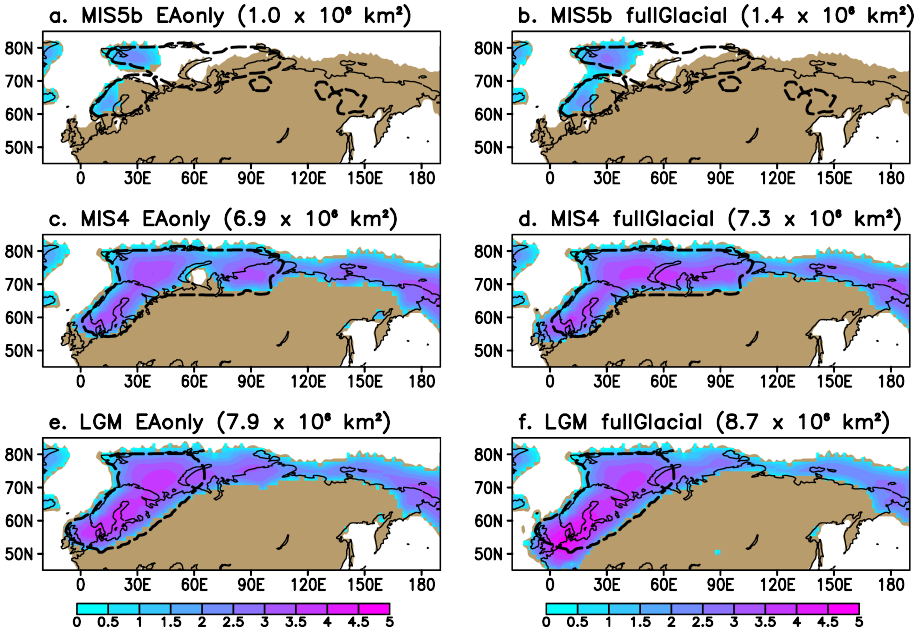

Figure 9. Same as Fig. 7 but using the climate forcing from the atmospheric simulations with BO2009 OHT.

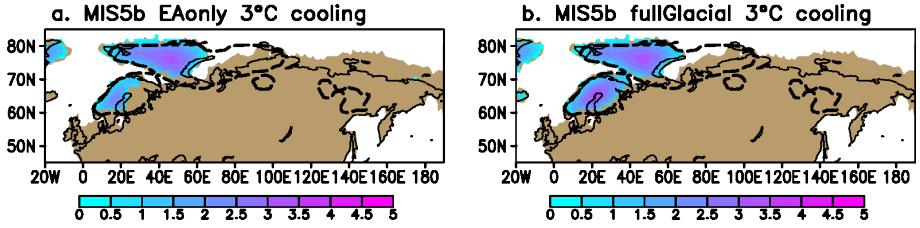

Figure 10. Simulated equilibrium ice thickness in Eurasia (shading; in km) using the MIS5b (with PI OHT) climate forcing from the EAonly (a,c) and fullGlacial (b,d) simulations. In (a,b), the simulations were initialized with the reconstructed ice-sheet topography from Kleman et al. (2013), and in (c,d) the JJA surface temperature was reduced by 3°C throughout the entire simulation.

Table 1. Top of the atmosphere insolation during the northern summer solstice (60°N; Berger and Loutre, 1991) and greenhouse gas concentrations (Petit et al., 1999; Spahni et al., 2005) in the time slice simulations.

	Insolation	CO_2	CH_4	N_2O
PI	475 W m^{-2}	280 ppm	760 ppb	270 ppb
MIS5b	505 W m^{-2}	210 ppm	450 ppb	240 ppb
MIS4	490 W m^{-2}	195 ppm	460 ppb	215 ppb
LGM	480 W m^{-2}	185 ppm	350 ppb	200 ppb

Table 2. Average summer (JJA) temperature in the Northern Hemisphere $\overline{T}_{NH}$, in Eurasia $\overline{T}_{EA}$ (average within the area 20°W, 180°E, 45°N and 90°N), and the average latitude of the zero-degree isotherm $\overline{\phi}_0$ in the PI OHT simulations.

	$\overline{T}_{NH}$	$\overline{T}_{EA}$	$\overline{\phi}_0$
Present-day	21.1°C	11.4°C	75°N
Pl	18.7°C	9.7°C	75°N
MIS5b EAonly	18.1°C	9.5°C	73° N
MIS5b fullGlacial	17.5°C	9.2°C	71°N
MIS4 EAonly	17.0°C	6.2°C	67°N
MIS4 fullGlacial	16.3°C	5.3°C	64°N
LGM EAonly	15.9°C	4.5°C	66°N
LGM fullGlacial	14.0°C	3.7°C	57°N